Engineered Science
DOI: https://dx.doi.org/10.30919/es1479

Functionalised Conductive Elastomers for Strain Monitoring of Seismic Isolation Bearings: Experiments and Molecular Simulations

Bangwei Wan,[1, 2, 4] Yang Yang,[1, 2, 4,*] Yong Yuan,[3] Rongxin Guo[1, 2, 4] and Xiaotao Yu[3]

Abstract

Conductive elastomers, commonly used in flexible electronics, enable real-time monitoring of deformation through changes in output resistance in response to signal variations. However, conductive elastomers often exhibit a shoulder peak effect in their output resistance response, which significantly compromises the stability of monitoring and limits their practical application. In this study, the cross-linked structure of elastomeric silicone rubber (VMQ) was modified using C-glue (VPS), and polyvinyl pyrrolidone (PVP)-functionalized multi-walled carbon nanotubes (MWCNT) were incorporated as conductive fillers (MP) to generate electrostatic repulsion and enhance dispersion within the matrix, forming a functionalized conductive elastomer. The results showed that the hysteresis area in the resistance response signal of the functionalized elastomer was reduced by 88.72%, effectively eliminating the shoulder peak effect. The mechanism behind the formation and removal of the shoulder peak effect was elucidated through a combination of experimental analysis and molecular dynamics simulations. The tensile strength and elongation at break of the functionalized conductive elastomer were increased by 69.44% and 50.91%, respectively, which endowed it with excellent strain-sensing properties, including a deformation sensitivity (gauge factor, GF = 16.92) and a response time of 262 ms. This elastomer was successfully applied for strain monitoring of seismic isolation bearings, with no shoulder peak effect observed during the process. It was capable of detecting residual deformation during the bi-directional shear loading, providing a more accurate assessment of cumulative damage and performance degradation within the seismic isolation bearings. This novel functionalized conductive elastomer demonstrates a significant potential for structural health monitoring in large-scale components.

Keywords: Conductive elastomer composites; Resistive response signal; Shoulder peak effect; Structural health monitoring.
Received: 24 March 2025; Revised: 21April 2025; Accepted: 25 April 2025.
Article type: Research article.

1. Introduction

Seismic isolation bearings are placed between a structure's superstructure and foundation to absorb earthquake-induced energy, playing a crucial role in the seismic resistance of buildings and bridges, and ensuring the safety of the superstructure.[1-4] However, these bearings are exposed to prolonged external loads and harsh environmental conditions, which can cause damage or even failure, compromising structural safety. Therefore, real-time deformation monitoring of seismic isolation bearings is critical. Currently, methods such as convolutional autoencoder (CAE) networks, active sensing technology, Bayesian-optimized deep neural networks, and wireless sensor networks (WSN) are employed to monitor the deformation of seismic isolation bearings.[5-7] However, these approaches often suffer from limitations, including poor resistance to environmental noise, inadequate real-time performance for vibration data acquisition, high installation and maintenance costs, and reduced accuracy in strain monitoring when training data is insufficient or feature selection is improper. Thus, there is a pressing need to develop a new, low-cost, high-stability intelligent composite material with synchronized deformation monitoring capabilities for

[1] *Faculty of Civil Engineering and Mechanics, Kunming University of Science and Technology, Kunming, 650500, China.*
[2] *Yunnan Key Laboratory of Disaster Reduction in Civil Engineering, Kunming, 650500, China.*
[3] *School of Civil and Hydraulic Engineering, Hua zhong University of Science and Technology, Wuhan, 430074, China.*
[4] *International Joint Laboratory for Green Construction and Intelligent Maintenance of Yunnan Province, Kunming, 650500, China*
**Email:* yangyang0416@kust.edu.cn (Y. Yang)

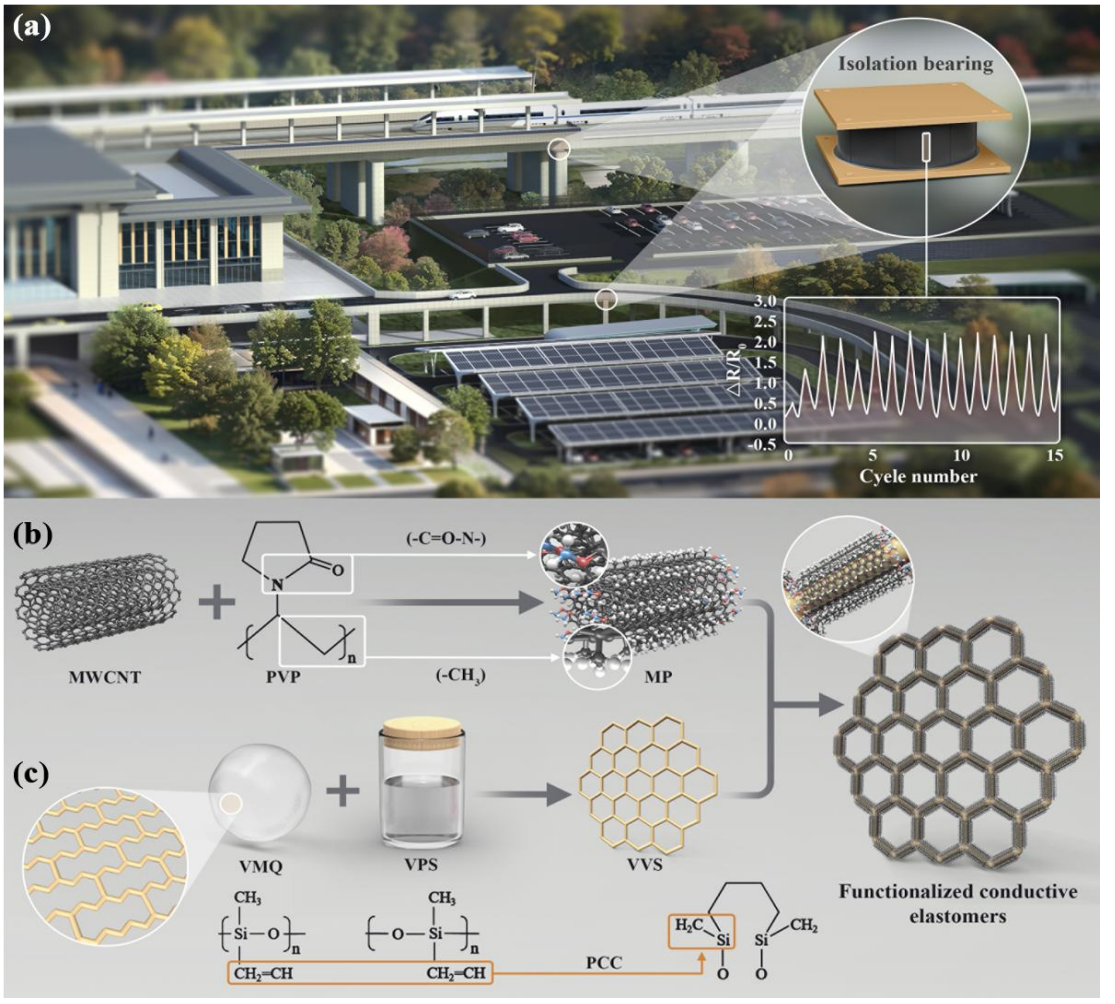

Fig. 1: (a) Scenario diagram of the application of seismic isolation bearings, (b) Mechanism diagram of functionalized MWCNT, and (c) Mechanism diagram of altering the original cross-linking structure of VMQ.

real-time strain monitoring of seismic isolation bearings, as illustrated in Fig. 1(a).

Elastomers are known for their impact resistance, light weight, and ease of processing, making them ideal matrices for new smart composites. At the same time, seismic isolation bearings are usually made of rubber, and the rubber in elastomers is compatible with seismic isolation rubber bearings, making them an ideal matrix for strain monitoring of seismic isolation bearings.[8-17] In recent years, conductive fillers such as multi-walled carbon nanotubes (MWCNT),[18,19] graphene (GR),[20-22] and conductive carbon black (CB),[23,24] have been incorporated into elastomers to impart conductive properties. This resistance/strain response characteristic enables real-time structural deformation monitoring, based on the functional relationship between the resistance and deformation of the conductive elastomer. Such monitoring is widely applied in areas like human body monitoring and structural health assessment.[25-28] However, conductive elastomers often exhibit a shoulder peak effect in their resistance response signal.[9,19,29-34] The shoulder peak effect refers to the nonlinear resistance signal observed during cyclic loading-unloading, where the main peak occurs at the maximum strain in tension, and a shoulder peak appears during unloading, as shown in Fig. S1. The occurrence of the shoulder peak effect has two main implications for the monitoring field. It distorts the resistance response signal, leading to an irreversible offset in the resistance change. This undermines strain monitoring accuracy, affecting the stability and consistency of the conductive elastomer's output signal. In long-term monitoring of large engineering structures, particularly during large deformation monitoring, the shoulder peak effect can mask actual damage signals, increasing potential safety risks.

Additionally, under dynamic loading, the shoulder peak effect exacerbates signal noise, further reducing the effectiveness and accuracy of real-time monitoring. The shoulder peak effect significantly undermines the stability of conductive elastomers in monitoring applications, hindering their development in the field. To address this, researchers have attempted various strategies, such as reducing residual strain, adjusting the dispersion of carbon nanomaterials, improving the negative Poisson's ratio of the material, and pre-stretching the elastomer to mitigate the shoulder peak effect.[35-39] However, these approaches often require specialized equipment, large quantities of chemical reagents, and complex designs. Thus, a simpler and more efficient preparation

method is needed to eliminate the shoulder peak effect in conductive elastomers. The self-assembly strategy has been used in the field of flexible strain sensors, and the performance of strain-sensing materials can be effectively improved by modifying the conductive fillers and substrates. For example, Ji *et al*.[40] prepared carbon nanotube whiskers (CNW)@n-AI_2O_3 micro- and nano- scale multilevel hybrid network structures by electrostatic self-assembly. Wang *et al*.[41] prepared highly conductive porous elastomers using a self-assembled solid-phase transition dual template (S-PTDT). Liu *et al*.[42] prepared boron nitride/nanodiamond (ND/KBN) honeycomb networks via an electrostatic self-assembly ice template method. Moreover, molecular dynamics (MD) simulation[43-45] is an effective computational tool for studying the physical behavior and molecular interactions of materials at the atomic level. MD simulations can complement experimental studies and provide a theoretical basis for eliminating the shoulder peak effect.

This research used a self-assembly method to adsorb alkyl and pyrrolidone groups from polyvinylpyrrolidone (PVP) onto the surface of MWCNT. This created synergistic mechanisms of spatial isolation and electrostatic repulsion, preventing MWCNT aggregation. Additionally, C-glue (VPS) was introduced into VMQ to modify its original crosslinking structure, increase its reactive sites, and enhance the crosslinking density of the conductive network. This process led to the formation of a self-assembled functional conductive elastomer, which effectively eliminates the shoulder peak effect and improves the stability of the elastomer during monitoring. The causes of the shoulder peak effect and its elimination mechanism were investigated through a combination of experimental and MD simulations. The developed conductive elastomer was successfully applied to strain monitoring of seismic isolation bearings.

2. Experiments

2.1 Materials

Materials in Supporting Information S1.1.

2.2 Preparation of functional conductive elastomer composites

Preparation process of conductive elastomer composites in support of information S1.2.

2.3 Characterization

Characterization test in support of information S1.3

2.4 MD simulation modeling and methods

Modeling Methodology and Models in Support of Information S1.4.

3. Results and discussion

3.1 Design of functionalized conductive elastomers

First, the functionalized conductive filler (MP) was created by adsorbing the methyl group (-CH_3) from PVP with the amide group (-C=O-N-) onto the surface of MWCNT. This process prevents MWCNT aggregation through electrostatic repulsion and spatial isolation, thereby promoting a better dispersion of MP within the matrix, as shown in Fig. 1(b). Next, the original cross-linking structure of VMQ was altered by introducing C-glue (VPS), which formed multiple centralized cross-linking points. This transition from a linear to a centralized cross-linking structure resulted in the creation of a new three-dimensional network (VVS system), as shown in Fig. 1(c). Finally, through temperature and shear synergism during the mixing process, MP and VVS were homogeneously combined to form the functionalized conductive elastomer. The detailed formation process and mechanism are described in section S2.1 (see supporting information).

3.2 Mechanism of generation and elimination of shoulder peak effect

Figs. 2(a-d) show the resistance response signals of MV, MVS, MPV, and MPVS under varying strains. It is clear that MV, MVS, and MPV exhibit nonlinear resistance responses, which compromise the stability of the conductive elastomer during monitoring. However, MPVS displays a stable, linear resistance response across different strain conditions, as shown in Fig. 2(d). To explain the mechanism behind the shoulder peak effect, the 5th cycle resistance signals at 10% strain were extracted from Figs. 2(a-d) for analysis, as illustrated in Figs. 2(e-k). There are three key observations: (1) Figs. 2(e-g) illustrates the 5th cycle resistance signals for MV, MVS, and MPV at 10% strain. When strain is applied, the distance between the conductive fillers and the substrate increases, severely damaging the conductive network, resulting in a sharp rise in resistance (AB). Upon unloading, due to the viscoelasticity of the elastomer,[46] the reconstruction of the conductive network lags behind the unloading process, causing a sudden increase in resistance (CD). (2) As shown in Fig. 2(i), the conductive filler is attached to the elastomer's molecular chain crosslinked network. When strain is applied, the crosslinking points of the molecular network inside the conductive elastomer are disrupted, increasing the distance between the conductive fillers and raising the resistance, as shown in Fig. 2(j). Upon unloading, the crosslinking network is reconstructed, but the conductive fillers slip along the molecular chain, causing a delayed change in the conductive network and scattering the fillers, as shown in Fig. 2(k). (3) Fig. S11(a-f) shows the TEM and SEM images of MV, MVS, and MPV. It is evident that the conductive fillers in all three elastomers are significantly agglomerated, forming localized aggregation regions that create obstacles to charge transfer. This results in a sudden change in electrical resistance when strain occurs, triggering a drastic shift in resistance. The shoulder peak effect can thus be attributed to four main factors: (1) Competition between the elastomer's viscoelasticity and the conductive network reconstruction process. (2) Insufficient crosslinking within the elastomer's molecular chain network, leading to weak

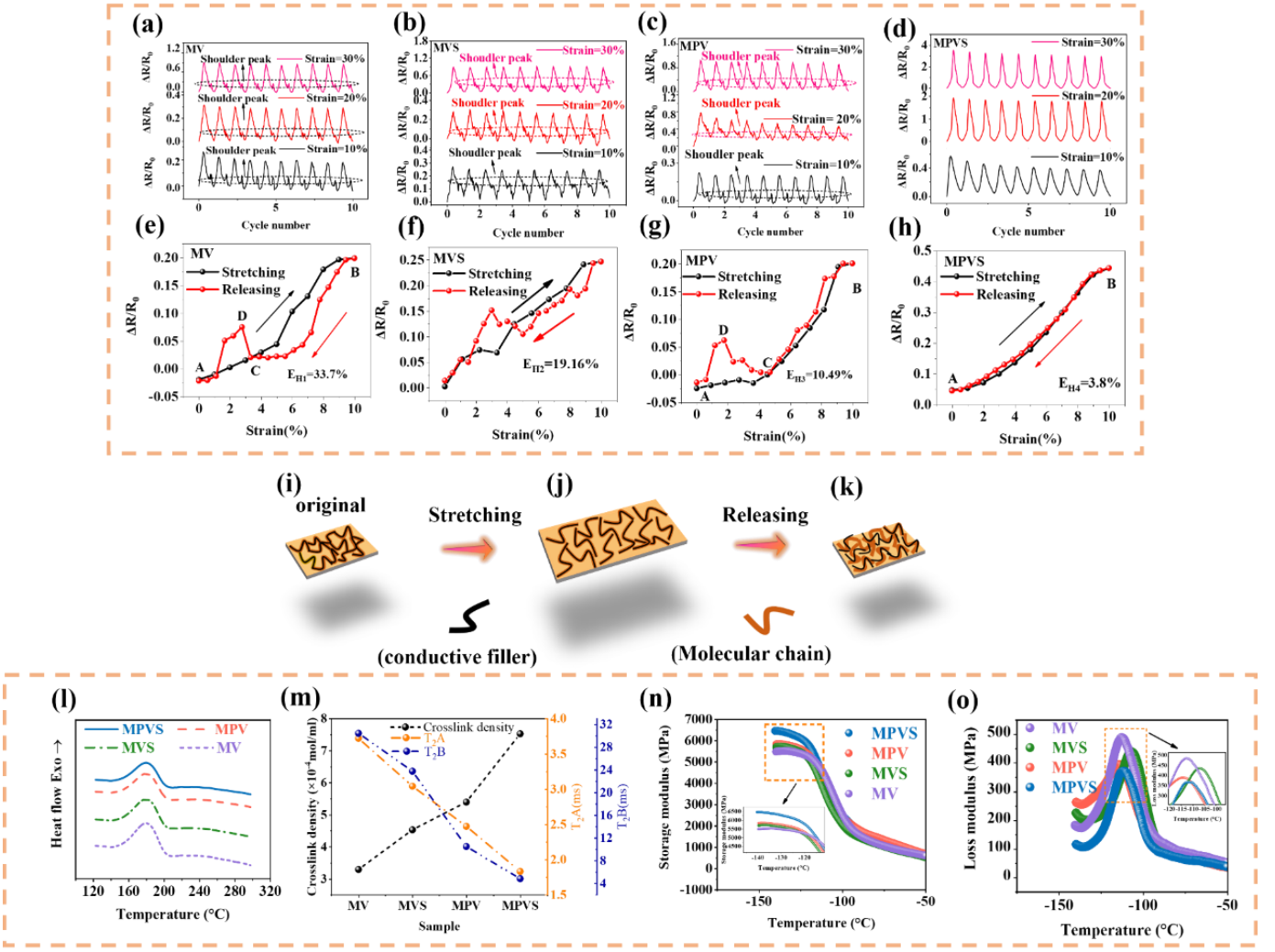

Fig. 2: (a~d) Resistive response signal plots of MV, MVS, MPV, MPVS, (e-h) the resistance/strain response of four conductive elastomers strained at 10% during the 5th cycle, (i~k) Mechanism plots of molecular chains inside the conductive elastomers during stretch-unloading, (l) DSC curves of MV, MVS, MPV, MPVS, (m) Crosslink density versus T_2 relaxation time plots, (n) Energy storage modulus of four conductive elastomers, and (o) Loss modulus of four conductive elastomers.

recovery of the conductive network during deformation. (3) Poor interfacial interaction between the conductive filler and elastomer, causing slippage between the two during strain unloading and large resistance hysteresis. (4) Poor dispersion of the conductive filler in the elastomer causes it to aggregate into clusters or form discontinuous conductive networks. Under strain, the local conductive channels experience sudden changes due to filler aggregation or lack of connectivity, leading to nonlinear fluctuations in the resistance response. To further elucidate the elimination of the shoulder peak effect, the following five methods were employed to analyze it:

(1) The hysteresis area of the resistance response signals for the four conductive elastomers is evaluated using Equation (1):

$$E_H = \frac{|E_S - E_R|}{E_S} \quad (1)$$

where E_S and E_R represent the areas under the tensile and unloaded resistance response curves, respectively. E_{H1}, E_{H2}, E_{H3}, E_{H4} correspond to the hysteresis areas of MV, MVS, MPV, and MPVS, respectively. A larger E_H value indicates a poorer recovery of the resistance response signal.[47] From Fig. 2(e-h), we observe the following values: E_{H1} =33.7%, E_{H2}=19.16%, E_{H3}=10.49%, E_{H4}=3.8%. The lag area of the MPVS resistance response is reduced by 88.72%. In addition, the viscoelasticity of the rubber was also evaluated using the Tan δ of the Rubber Processing Analyser (RPA).[48] The Tan δ values of four conductive elastomers at a strain of 1-10% are shown in Fig. S11, and the average values of MV, MVS, MPV, and MPVS were calculated to be 0.94, 0.92, 0.91, and 0.86, respectively, which are denoted as Tan δ_{A1}, Tan δ_{A2}, Tan δ_{A3}, and Tan δ_{A4}, respectively. Meanwhile, based on the calculated E_H, the intensity of competition between the rubber matrix viscoelasticity and the conductive network reconstruction is denoted as VR and presented by Equation (2):

$$\mathrm{VR} = \frac{E_H}{\mathrm{Tan}\ \delta_A} \quad (2)$$

A larger VR represents a stronger intensity of competition between the rubber viscoelasticity and the conductive network

reconstruction, and the results of the calculations are shown in Table S1. The results show that the VR of MPVS conductive elastomer is lower than that of the other three conductive elastomers. This proves that MPVS has a good ability to recover the resistance response.

(2) Fig. S11(g-h) shows the TEM and SEM images of MPVS, where the white tubes represent the conductive filler and the black areas represent SiO_2. Compared to the other three conductive elastomers in Fig. S11(a-f), it is clear that the MP in MPVS is uniformly dispersed throughout the matrix. To further assess the dispersion of the conductive elastomers, the roughness, adhesion, and 3D profile of the materials were analyzed using AFM, as shown in Fig. S13(a-h). The results reveal that the roughness and adhesion of MV, MVS, and MPV are higher than those of MPVS, indicating that the surface fluctuations in MV, MVS, and MPV are more pronounced, with conductive fillers more heavily agglomerated within the matrix. In contrast, MPVS exhibits smoother surface fluctuations, promoting a better continuity of the MP within the matrix. The specific roughness values are provided in Table S2. This phenomenon is also clearly visible in the 3D contour maps shown in Fig. S14(a-d).

Additionally, the dispersion of the four conductive elastomers was evaluated by RPA. Fig. S15 presents the energy storage modulus (G′), loss factor (Tan δ), and complex viscosity (η*) of the elastomers under strain conditions. Fig. S15(a) illustrates the G′ of MV, MVS, MPV, and MPVS, showing a linear decrease in G′ for all four materials. This decrease is attributed to the disruption of the conductive network as strain increases, known as the Payne effect,[49] which is commonly used to assess filler agglomeration in the matrix.[50] The ΔG′ value, defined as the difference between G′ at maximum and minimum strain (ΔG′ = G′ at 99.98% strain - G′ at 9.98% strain), serves as the assessment criterion. A larger ΔG′ indicates a stronger Payne effect, more severe filler agglomeration, poorer dispersion, and a more unstable conductive network. From Fig. S15(a), the ΔG′ values for MV, MVS, MPV, and MPVS are 39.71, 35.29, 35.29, and 32.44, respectively, indicating that MPVS exhibits superior dispersion of MP. Fig. S15(b) shows that the Tan δ of MV, MVS, and MPV is significantly higher than that of MPVS. This is attributed to the aggregation of conductive fillers in MV, MVS, and MPV, which increases internal friction and energy loss, resulting in a higher hysteresis loss when the conductive network is damaged.

Fig. S15(c) shows the complex viscosity (η*) of the conductive elastomer, which reflects the rheological properties of the conductive elastomer during processing.[51,52] When the η* of the conductive elastomer is high, the rheological resistance of the conductive elastomer increases, causing the conductive fillers to aggregate into clusters in the elastomer. When the η* of the conductive elastomer is low, it indicates that the conductive filler has a better flowability in the elastomer, a less internal friction, and the conductive filler is uniformly dispersed in the conductive elastomer. The η* of MPVS is notably lower than that of MV, MVS, and MPV, which suggests that the conductive fillers in MV, MVS, and MPV are agglomerated, affecting the fluidity within the matrix, increasing the internal friction, and raising η*. These findings indicate that the MP in MPVS have excellent dispersion properties.

(3) DSC and NMR techniques were employed to evaluate the degree of cross-linking in the conductive elastomers. Fig. 2(l) shows the DSC curves for MV, MVS, MPV, and MPVS, where the exothermic response is associated with the cross-linking process of the elastomers.[53] It is evident that the exothermic curve for MPVS is higher than those for the other three conductive elastomers, indicating that the cross-linking reaction sites in MPVS are more numerous, leading to a denser, more highly cross-linked conductive network. Fig. 2(m) presents the trends in crosslink density and T_2 relaxation time for MV, MVS, MPV, and MPVS. The crosslink density of MPVS is 56.34% higher than that of MV, suggesting the formation of new cross-linking points within MPVS. This results in a more stable, three-dimensional conductive network within the elastomer. Additionally, the T_2 relaxation time for MPVS is consistently shorter than those for MV, MVS, and MPV, further confirming the increased degree of cross-linking in MPVS.[54] The T_2 relaxation time inversion spectra for all four elastomers are shown in Fig. S16. The peaks for T_2A and T_2B in MPVS significantly shift towards shorter relaxation times, indicating an increase in cross-linking points within the molecular chain of the conductive elastomer. Moreover, the intensity of the T_2A signal for MPVS is lower than that for MV, MVS, and MPV, suggesting a quicker transition from free to cross-linked chains[53] due to the higher number of cross-linking reaction points in MPVS, as shown in Fig. S17.

(4) DMA and XPS were employed to evaluate the binding energy and molecular chain motion of the conductive elastomers. Fig. 2(n) and 2(o), along with Fig. S18, demonstrate the energy storage modulus, loss modulus, and loss factor (Tan δ) of MV, MVS, MPV, and MPVS as a function of temperature. As shown in Fig. 2(n), the energy storage modulus reflects the binding energy between the filler and the matrix, with a higher modulus indicating stronger interaction.[55] The energy storage modulus of MPVS is higher than that of other three conductive elastomers, suggesting a stronger interaction between the filler and the matrix in MPVS, as well as a higher degree of molecular chain confinement within the elastomer. Fig. 2(o) shows the loss modulus of four conductive elastomers, which reflects the internal friction and energy dissipation within the materials.[56] Stronger binding energy between the filler and the matrix reduces the interfacial slip and friction, thereby lowering the loss modulus. The loss modulus of MV, MVS, MPV, and MPVS are 488.4, 439.41, 394.11, and 369.92 MPa, respectively. The 24.25% reduction in loss modulus for MPVS indicates that the filler within MPVS forms a strong interface with the elastomer, significantly constraining the molecular chain movement.[57] Fig. S18 illustrates the Tan δ of four elastomers, which reflects

the motion of the molecular chains.[58] The peak value of Tan δ for MPVS is lower than that for MV, MVS, and MPV, suggesting that the molecular chain movement in MPVS is more restricted. In addition, T_g represents the glass transition temperature of the conductive elastomer, while T_{g1}, T_{g2}, T_{g3}, and T_{g4} refer to the glass transition temperatures of MV, MVS, MPV, and MPVS, respectively. T_{g1} of MPVS shifts significantly to the right compared to T_{g4}, T_{g3}, and T_{g2} of MV, MVS, and MPV. This shift is attributed to the strong interfacial binding energy, which restricts the free movement of the matrix's molecular chains and leads to the formation of regions with higher molecular chain constraints in MPVS.[57] To further evaluate the interfacial binding energy between the filler and matrix, XPS analysis was conducted. Fig. S19 and S20 show the C1s and O1s spectra for the four conductive elastomers, with characteristic peaks for C-C and Si-O bonds. The C-C and Si-O peaks for MPVS shift to higher binding energies (from 283.38 to 283.74 eV) for C-C and from 531.15 to 531.65 eV for Si-O, indicating a stronger filler-matrix interaction in MPVS.

(5) All-atom molecular dynamics simulations. To further explain the mechanism behind the elimination of the shoulder peak effect, MD simulations were used to calculate the mean square displacement (MSD), free volume fraction (FFV), radial distribution function (RDF), and pullout simulation binding energy. The specific modeling steps can be found in section (S1.4), and the models of VMQ, VPS, MWCNT, and MP are shown in Fig. S3(a-d). The AC models of MV, MVS, MPV, and MPVS are depicted in Fig. S4. MSD is used to evaluate the movement of conductive fillers within the elastomer molecular chains (S1.5). A lower MSD value indicates that the molecular chains are more constrained. As shown in Fig. 3(a), the MSD of MPVS is lower than that of MV, MVS, and MPV, indicating that MPVS has highly constrained regions, which restrict the movement of its molecular chains. RDF is used to assess the adsorption capacity between the elastomer and conductive fillers (S1.6). Fig. 3(b) shows that the average RDF of MPVS is higher than that of MV, MVS, and MPV, suggesting that MPVS exhibits a stronger adsorption between the conductive fillers (MP) and the molecular chains of the matrix. FFV reflects the ability of molecular chains to move within the conductive elastomer (S1.7). As shown in Fig. 3(c), the FFV of MPVS is reduced by 30.32% compared to MV, MVS, and MPV, indicating that the molecular chains in MPVS are more hindered and constrained than in the other elastomers.

Additionally, the interfacial bonding energies were calculated using pull-out simulations (S1.8) for MV, MVS, MPV, and MPVS, as shown in Fig. 3(d) and Fig. S21-S23. As the number of simulation frames increased, the interface between the conductive filler and the elastomer was disrupted. The calculated interfacial binding energies for each material at 1 Ps, 50 Ps, 100 Ps, 200 Ps, and 300 Ps are shown in Fig. 3(e). It is evident that the interfacial binding energies of MPVS are higher than those of MV, MVS, and MPV, indicating better interfacial interactions within MPVS. Furthermore, the interfacial binding energies of MPVS at 300 Ps are 67.56% higher than those of MV, MVS, and MPV, suggesting a stronger bonding between the conductive fillers and the molecular chains within MPVS, making it more difficult for the fillers to detach from the matrix. These MD simulation results are consistent with the findings from DMA and XPS experiments, confirming the enhanced interfacial interactions and better overall structural stability of MPVS.

In summary, by functionalizing commercial MWCNT and modifying the original cross-linking structure of VMQ, the MP inside MPVS generates electrostatic repulsion, which prevents MP from agglomerating within the matrix. At the same time, this modification increases the reaction sites on the molecular chains of MPVS, leading to more cross-linking points between the chains. This results in a higher cross-linking density and a greater degree of constraint on the formation of free chains within MPVS, converting them into cross-linked regions. As a result, the conductive cross-linked network structure inside MPVS is enhanced. When the conductive network is reconstructed, the movement of MP attached to the molecular chain of MPVS is restricted, forming spatial isolations within the conductive network. This strengthens the interfacial bonding interactions between MP and the molecular chain of MPVS and reduces the sudden rise in electrical resistance that occurs during strain unloading. Consequently, the shoulder peak effect is eliminated. Fig. S24 illustrates a schematic diagram of the internal cross-linked network of MPVS during stretch-unloading.

3.3 Force-electric response properties of conductive elastomers

Fig. 4(a) shows the stress-strain curves of MV, MVS, MPV, and MPVS. All four conductive elastomers exhibit a linear growth trend, with the curve for MPVS showing a steeper slope than those of MV, MVS, and MPV, indicating that MPVS has a superior deformation ability. Furthermore, the tensile strength and elongation at break of MPVS are increased by 69.44% and 50.91%, respectively. These improvements are attributed to the introduction of functionalized MP and VPS, which enhance the cross-linking network of MPVS and increase cross-linking points, strengthening the interactions between the filler and matrix. Fig. S25 (a~h) shows the cyclic stress-strain curves of MV, MVS, MPV, and MPVS. The hysteresis area of the stress-strain curves was evaluated using Equation (3):

$$H_R = \frac{L - L_R}{L} \tag{3}$$

where L is the area in tension and L_R is the area in unloading. The highest reduction in hysteresis for MPVS, at 49.95%, indicates a better elasticity compared to MV, MVS, and MPV. Fig. 4(b) illustrates the uniaxial resistance-strain response of MV, MVS, MPV, and MPVS at a strain of 100%. As strain increases, the resistance of all conductive elastomers rises. The sensitivity of the conductive elastomers is quantified using

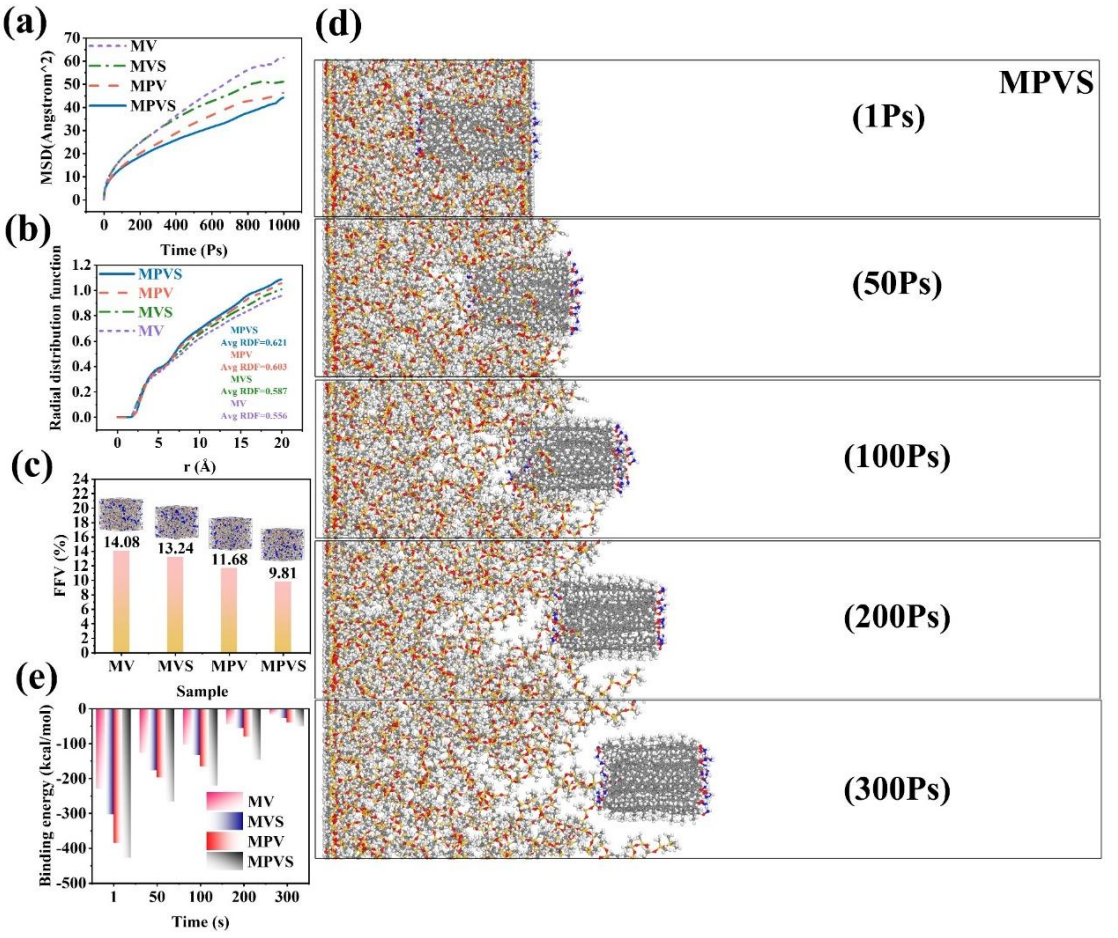

Fig. 3: (a) MSD of MV, MVS, MPV, MPVS, (b) RDF of MV, MVS, MPV, MPVS, (c) FFV of MV, MVS, MPV, MPVS, (d) Pulling and pulling the simulation process of MPVS, and (e) The pull-out simulation binding energy of MV, MVS, MPV, MPVS at frame numbers of 1, 50, 100, 200, 300 Ps.

gauge factor (GF) as shown by Equation (4):

$$GF = (\Delta R/R_0)/\varepsilon \quad (4)$$

where $\Delta R=R-R_0$, R_0 is the initial resistance, R is the test resistance, and ε is the strain. The maximum resistance variation and maximum GF variation of the four conductive elastomers are displayed in Fig. 4(c). The maximum resistance change and maximum deformation sensitivity for MPVS are increased by 79.02% and 83.98%, respectively, compared to MV, MVS, and MPV, indicating that MPVS has superior sensitivity and higher deformation responsiveness.

Fig. S26 shows the current-voltage (CV) curves for MV, MVS, MPV, and MPVS. As the voltage increases from 1 to 5 V, the current increases for all four materials, suggesting that they maintain stable resistance within this voltage range. Fig. 4(d) demonstrates that MPVS maintains a stable resistance response across all strains. Fig. 4(e) shows that the resistance recovery time of MPVS at a strain of 5% and a rate of 1000 mm/min is 262 ms, which is faster than that of other conductive elastomer materials.[59-64] Fig. 4(f) confirms that MPVS maintains a stable resistance response under various strain rates, proving that the resistance signal is not rate-dependent. Fig. 4(g~j) shows the results of 200 cycles of MPVS under strain, with no shoulder peak effect observed in the first 10 cycles or the last 190 cycles. To evaluate the long-term stability of MPVS resistive response, the material was tested for 5000 cycles at a strain of 60%, as shown in Fig. 4(k). MPVS gradually decreases in resistance with increasing cycles and finally flattens out. This is due to the viscoelasticity of the rubber itself,[46] which produces hysteresis effect and triggers the resistance hysteresis phenomenon.[20] The enlarged view reveals that no shoulder peak effect occurs during the 5000 cycles, indicating that MPVS maintains a stable resistive response signal over extended cycling.

3.4 Application of MPVS for monitoring of seismic isolation bearing

The sensing range and experimental design for seismic isolation bearing monitoring are detailed in Sections S2.2 and S2.3. Fig. 5(a-e) demonstrates the strain monitoring of lead core seismic isolation rubber bearing (LRB) under bidirectional shear deformation on a compression-shear machine using MPVS. It is evident that, under varying shear displacements, the output signals of MPVS deform synchronously with the LRB during the shear deformation. Conventional monitoring materials rarely withstand such large

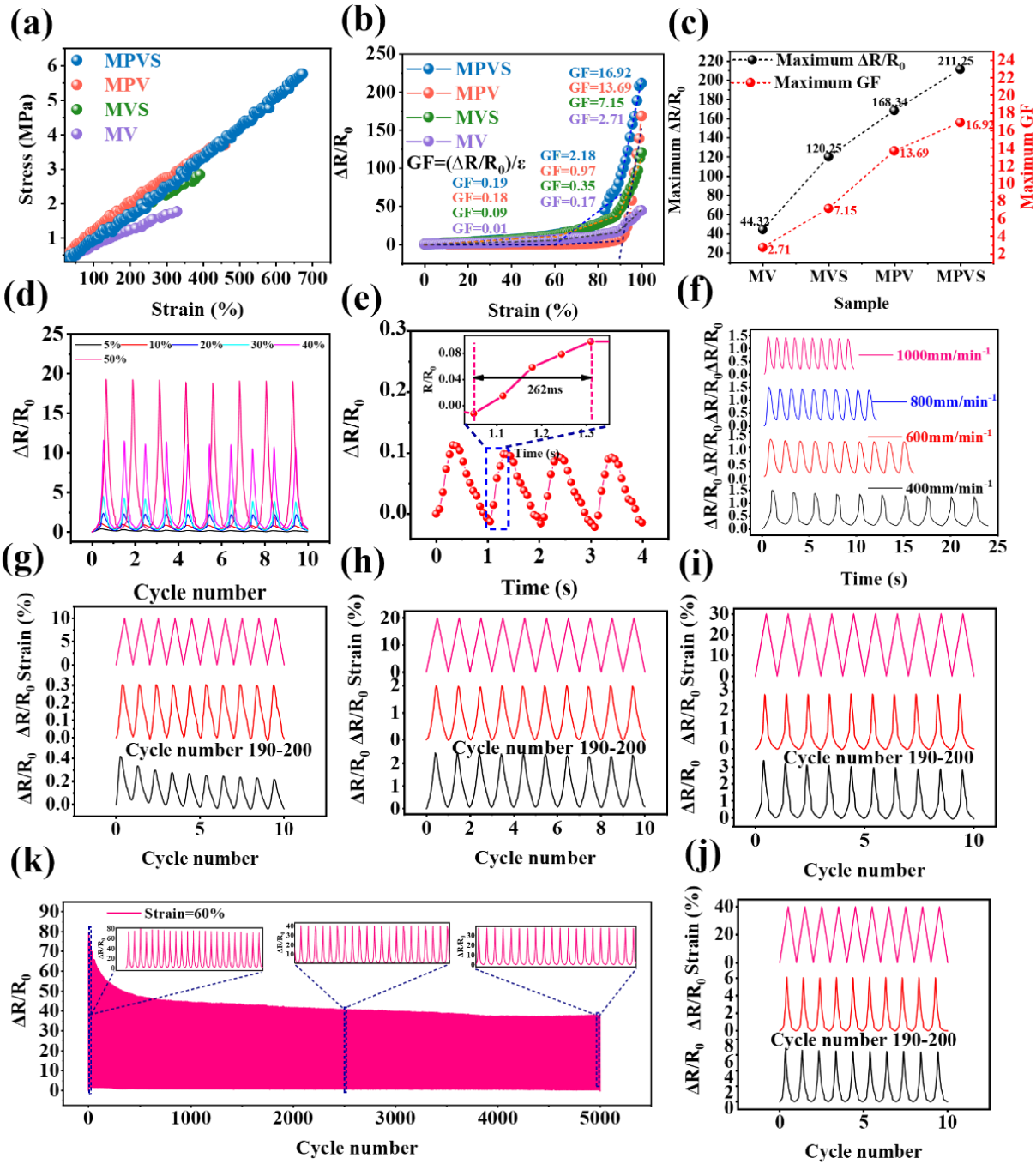

Fig. 4: (a) Stress-strain curves of MV, MVS, MPV, and MPVS, (b) Uniaxial resistance-strain response of MV, MVS, MPV, and MPVS at a strain of 100%, (c) Maximum resistance of four conductive elastomers with GF value change, (d) Plots of resistance response signals of MPVS at different strains, (e) Recovery time of the resistance response signals of MPVS at a strain of 5% and a rate of 1000 mm/min^{-1}, (f) Resistive response signal plots of MPVS at different rates, (g~j) Resistive response signal plots of MPVS for 200 cycles at strains of 10%, 20%, 30%, and 40%, and (k) Resistive response signal plots of MPVS for 5,000 cycles at a strain of 60%.

deformations while maintaining complete synchronization between resistance and strain. Furthermore, compared to other monitoring materials used in physiological, mechanical, and large-scale structural monitoring, this conductive elastomer exhibits no shoulder peak effect, as statistically demonstrated in Table S3. Real-time videos of different shear displacements are available in V1-V4 (supporting information). Notably, distinct large and small peaks of varying heights emerge in the resistance response signals under different shear displacements. This phenomenon results from residual deformation caused by previous bidirectional shear cycles, which accumulates with subsequent shear deformations, leading to sudden increases in the resistance response signal. This finding confirms that MPVS can effectively monitor residual strain in objects subjected to large deformations, enabling timely detection of potential damage or deformation

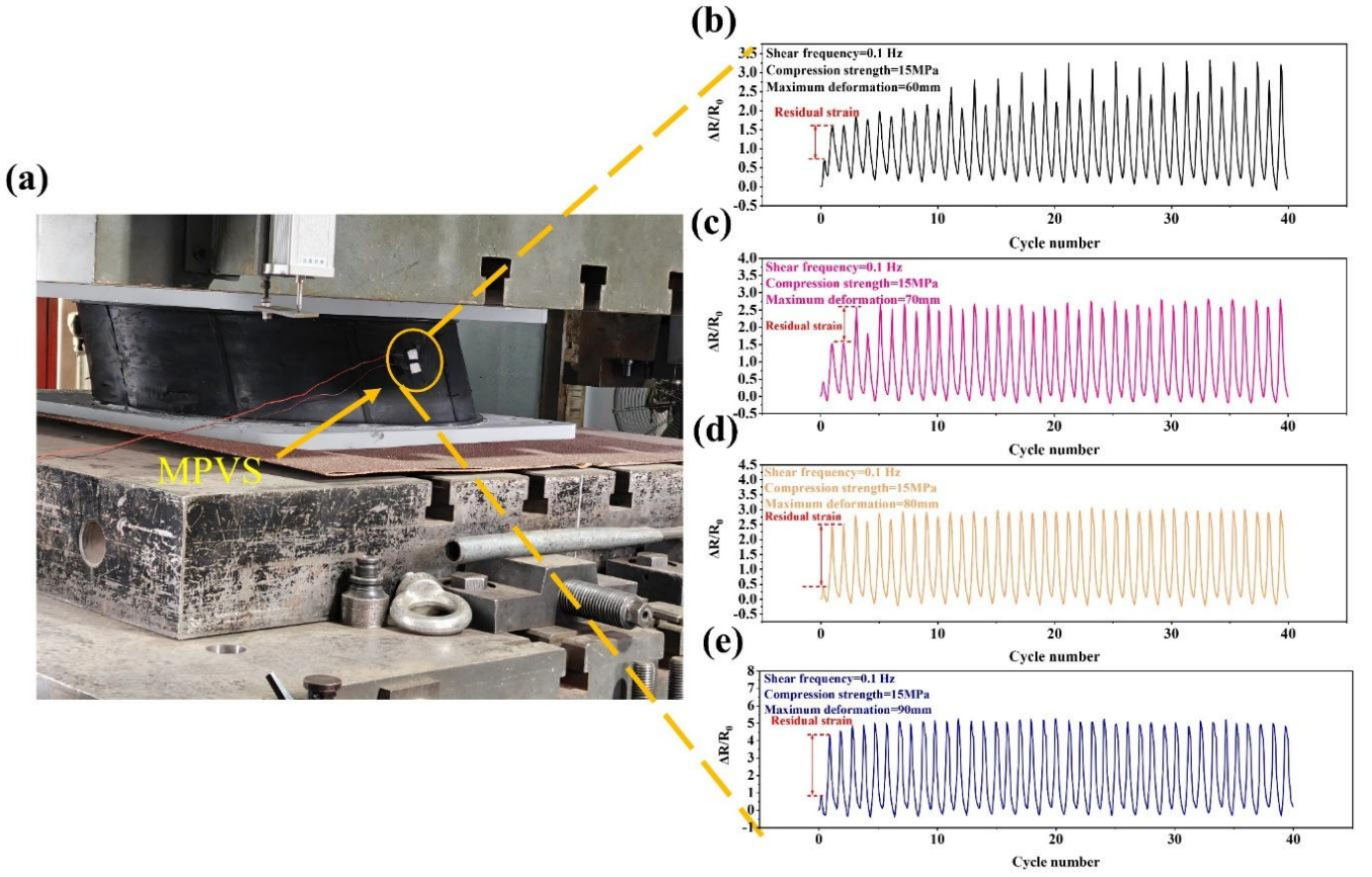

Fig. 5: (a) MPVS strain monitoring of seismic isolation bearings undergoing bi-directional shear deformation, and (b~e) The strain monitoring of MPVS on LRB under bi-directional shear conditions from 60 to 90 mm.

to ensure structural safety. This capability significantly enhances the implementation of intelligent monitoring for large-scale components.

4. Conclusion

In this work, we employed a self-assembly strategy to successfully prepare novel self-assembled functionalized conductive elastomers MPVS, which are used for strain monitoring of seismic isolation bearings through the output resistive response signal. The successful adsorption of alkyl and pyrrolidone groups from PVP onto commercial MWCNT creates electrostatic repulsion, resulting in highly dispersed MP conductive fillers. Meanwhile, C-glue (VPS) was used to alter the cross-linking structure of the original VMQ, increase its reactive sites, and enhance its cross-linking degree, resulting in a highly cross-linked VVS matrix. MP and VVS were mixed under strong shear forces to obtain a highly stable MPVS with good dispersion performance. MPVS overcame the shoulder peak effect that commonly occurs during the output of resistive response signals in conductive elastomers. The causes of the shoulder peak effect were analyzed, and its elimination mechanism was explained using a combination of experimental and molecular dynamics simulation methods. MPVS also exhibited excellent force-electric response performance, including an increase in tensile strength and elongation at break by 69.44% and 50.91%, respectively, a reduction in stress-strain hysteresis area by 49.95%, and an increase in resistance change and deformation sensitivity by 79.02% and 83.98%, respectively. Additionally, during strain monitoring of the seismic isolation bearing, no shoulder peak effect was observed, and the resistance response signal remained stable. The self-assembled functionalized conductive elastomer opens up new application prospects in the field of large component monitoring. However, due to the viscoelastic properties of the rubber matrix, it exhibits a significant resistance hysteresis during the resistance/strain response, which affects their stability during the monitoring process. Therefore, how to minimise the effect of the viscoelasticity of the rubber matrix on the resistance/strain response signal will be a key challenge for future research.

Acknowledgment

This work was supported by the National Natural Science Foundation of China (Grant No 52368043).

Conflict of Interest

There is no conflict of interest.

Supporting Information

Not applicable.

References

[1] D. De Domenico, E. Gandelli, V. Quaglini, Adaptive isolation system combining low-friction sliding pendulum bearings and SMA-based gap dampers, *Engineering Structures*, 2020, **212**, 110536, doi: 10.1016/j.engstruct.2020.110536.

[2] P. Clemente, G. Bongiovanni, G. Buffarini, F. Saitta, M. G. Castellano, F. Scafati, Effectiveness of HDRB isolation systems under low energy earthquakes, *Soil Dynamics and Earthquake Engineering*, 2019, **118**, 207-220, doi: 10.1016/j.soildyn.2018.12.018.

[3] Z. Shao, W. Bai, J. Dai, R. Liu, Research on compressive behavior of thick rubber bearings for mitigating train-induced structural vibration, *Engineering Structures*, 2024, **315**, 118444, doi: 10.1016/j.engstruct.2024.118444.

[4] Z. Shao, W. Bai, J. Dai, H. Yu, B. Wu, J. Liang, Research on the effectiveness of a new-type bearing for structural seismic and vibration dual control, *Structures*, 2024, **62**, 106188, doi: 10.1016/j.istruc.2024.106188.

[5] M. Zhang, T. Guo, R. Zhu, Y. Zong, Z. Liu, W. Xu, Damage identification of seismic-isolated structure based on CAE network using vibration monitoring data, *Engineering Structures*, 2023, **283**, 115873, doi: 10.1016/j.engstruct.2023.115873.

[6] Y. Zeng, C. Deng, F. Xiong, H. Peng, Y. Xu, Y. Liu, DetachSense rubber bearing for convenient axial load prediction using active sensing and Bayesian-optimized deep neural network, *Engineering Structures*, 2024, **315**, 118503, doi: 10.1016/j.engstruct.2024.118503.

[7] D. M. Siringoringo, Y. Fujino, M. Suzuki, V. Mehta, Implementation of wireless sensor network for continuous seismic monitoring of isolated cable-stayed bridge, *Journal of Bridge Engineering*, 2022, **27**, 04022011, doi: 10.1061/(asce)be.1943-5592.0001813.

[8] Q. Zhu, W. Liao, C. Sun, X. Qin, F. Zhang, H. Ji, Y. Li, Z. Wen, X. Sun, Highly stretchable, conductive, and wide-operating temperature ionogel based wearable triboelectric nanogenerator, *Nano Research*, 2023, **16**, 11638-11645, doi: 10.1007/s12274-023-5851-3.

[9] W. Yao, Y. Yan, J. Sun, Z. Zhang, W. Sun, W. Huang, J. Cheng, H. Zhao, M. Xie, Q. Sun, G. Huang, X. Lin, Mechanically durable superhydrophobic strain sensors with high biocompatibility and sensing performance for underwater motion monitoring, *ACS Applied Materials & Interfaces*, 2024, **16**, 6548-6561, doi: 10.1021/acsami.3c14327.

[10] H. Feng, P. Liu, X. Guo, J. Li, Y. Sun, S. Wu, R. Hu, Z. Liu, H. Tian, Y. Ma, C. Liu, H. Huang, F. Teng, X. Tang, A. Yang, A. Song, X. Yang, Y. Huang, PSS modified by 3-aminopropyltrimethoxysilane linking large-area GNPs/PSS to silicone rubber with stable interface combination for high sensitivity flexible resistive sensor, *Chemical Engineering Journal*, 2023, **465**, 143009, doi: 10.1016/j.cej.2023.143009.

[11] B. Wan, Y. Yang, R. Guo, Z. Fan, P. Deng, S. Zhang, Effect of vulcanization on the electro-mechanical sensing characteristics of multi-walled carbon nanotube/silicone rubber composites, *Polymers*, 2023, **15**, 1412, doi: 10.3390/polym15061412.

[12] H. Wu, C. Wang, L. Liu, Z. Liu, J. He, C. Zhang, J. Duan, Bioinspired stretchable strain sensor with high linearity and superhydrophobicity for underwater applications, *Advanced Functional Materials*, 2025, **35**, 2413552, doi: 10.1002/adfm.202413552.

[13] N. Wang, X. Yang, X. Zhang, Ultrarobust subzero healable materials enabled by polyphenol nano-assemblies, *Nature Communications*, 2023, **14**, 814, doi: 10.1038/s41467-023-36461-9.

[14] Y. Lv, C. Li, Z. Yang, M. Gan, Y. Wang, M. Lu, X. Zhang, L. Min, Monomer trapping synthesis toward dynamic nanoconfinement self-healing eutectogels for strain sensing, *Advanced Science*, 2024, **11**, 2410446, doi: 10.1002/advs.202410446.

[15] M. Cheng, K. Tian, T. Qin, Q. Li, H. Deng, Q. Fu, Recent development on the design, preparation, and application of stretchable conductors for flexible energy harvest and storage devices, *SusMat*, 2024, **4**, e204, doi: 10.1002/sus2.204.

[16] A. Seilkhan, An overview of green applications of natural products for pharmaceutical, biofuel, and rubber industries: case study of Kazakh dandelion (taraxacum kok-saghyz Rodin.), *ES Energy & Environment*, 2024, **25**, 1171, doi: 10.30919/esee1171.

[17] S. Chanthee, C. Asavatesanupap, D. Sertphon, T. Nakkhong, N. Subjalearndee, M. Santikunaporn, Surface transformation of carbon nanofibers *via* co-electrospinning with natural rubber and Ni doping for carbon dioxide adsorption and supercapacitor applications, *Engineered Science*, 2024, **27**, 975, doi: 10.30919/es975.

[18] Z. Fu, Q. Chen, J. He, S. Li, R. Ming, Y. Wei, Y. Xu, J. Liu, L. Zhang, A synergistic effect of MXene/MWCNT enables self-healable and low percolation elastomer sensor: A combined experiment and all-atom molecular dynamics simulation, *Composites Science and Technology*, 2023, **242**, 110155, doi: 10.1016/j.compscitech.2023.110155.

[19] J. Tang, Y. Wu, S. Ma, T. Yan, Z. Pan, Flexible strain sensor based on CNT/TPU composite nanofiber yarn for smart sports bandage, *Composites Part B: Engineering*, 2022, **232**, 109605, doi: 10.1016/j.compositesb.2021.109605.

[20] H. Yang, X. Yao, Z. Zheng, L. Gong, L. Yuan, Y. Yuan, Y. Liu, Highly sensitive and stretchable graphene-silicone rubber composites for strain sensing, *Composites Science and Technology*, 2018, **167**, 371-378, doi: 10.1016/j.compscitech.2018.08.022.

[21] H. Yang, L. Yuan, X. Yao, Z. Zheng, D. Fang, Monotonic strain sensing behavior of self-assembled carbon nanotubes/graphene silicone rubber composites under cyclic loading, *Composites Science and Technology*, 2020, **200**, 108474, doi: 10.1016/j.compscitech.2020.108474.

[22] H. Han, H. Sun, F. Lei, J. Huang, S. Lyu, B. Wu, M. Yang, C. Zhang, Z. Zhang, D. Sun, Flexible ethylene-vinyl acetate copolymer/fluorographene composite films with excellent thermal conductive and electrical insulation properties for thermal management, *ES Materials & Manufacturing*, 2021, **15**, 53-64, doi: 10.30919/esmm5f523.

[23] K. Y. Chung, B. Xu, Z. Li, Y. Liu, J. Han, Bioinspired ultra-stretchable dual-carbon conductive functional polymer fiber

materials for health monitoring, energy harvesting and self-powered sensing, *Chemical Engineering Journal*, 2023, **454**, 140384, doi: 10.1016/j.cej.2022.140384.
[24] J. Yuan, Q. Li, L. Ding, C. Shi, Q. Wang, Y. Niu, C. Xu, Carbon black/multi-walled carbon nanotube-based, highly sensitive, flexible pressure sensor, *ACS Omega*, 2022, **7**, 44428-44437, doi: 10.1021/acsomega.2c06548.
[25] J. Wang, Z. He, Z. Du, X. Cheng, H. Wang, X. Du, Highly stretchable $Ti_3C_2T_x$ MXene-integrated phase change films for solar-thermal harvesting and infrared stealth, *ACS Sustainable Chemistry & Engineering*, 2023, **11**, 13187-13197, doi: 10.1021/acssuschemeng.3c03543.
[26] Y. Li, D. Yang, Z. Wu, F. Gao, X. Gao, H. Zhao, X. Li, Z. Yu, Self-adhesive, self-healing, biocompatible and conductive polyacrylamide nanocomposite hydrogels for reliable strain and pressure sensors, *Nano Energy*, 2023, **109**, 108324, doi: 10.1016/j.nanoen.2023.108324.
[27] M. N. Alam, V. Kumar, D. J. Lee, J. Choi, Synergistically toughened silicone rubber nanocomposites using carbon nanotubes and molybdenum disulfide for stretchable strain sensors, *Composites Part B: Engineering*, 2023, **259**, 110759, doi: 10.1016/j.compositesb.2023.110759.
[28] W. Hong, X. Guo, X. Li, T. Zhang, X. Zhu, J. He, R. Zhang, S. Yang, Y. Shao, Y. Fang, Z. Yin, X. Sun, J. Hu, Q. Hong, Y. Zhao, Fishbone and nettle fiber inspired stretchable strain sensor with high sensitivity and wide sensing range for wearable electronics, *Chemical Engineering Journal*, 2024, **492**, 152281, doi: 10.1016/j.cej.2024.152281.
[29] Y. Zheng, Y. Li, K. Dai, Y. Wang, G. Zheng, C. Liu, C. Shen, A highly stretchable and stable strain sensor based on hybrid carbon nanofillers/polydimethylsiloxane conductive composites for large human motions monitoring, *Composites Science and Technology*, 2018, **156**, 276-286, doi: 10.1016/j.compscitech.2018.01.019.
[30] P. Ahuja, S. K. Ujjain, K. Urita, A. Furuse, I. Moriguchi, K. Kaneko, Chemically and mechanically robust SWCNT based strain sensor with monotonous piezoresistive response for infrastructure monitoring, *Chemical Engineering Journal*, 2020, **388**, 124174, doi: 10.1016/j.cej.2020.124174.
[31] S. Salaeh, A. Das, K. W. Stöckelhuber, S. Wießner, Fabrication of a strain sensor from a thermoplastic vulcanizate with an embedded interconnected conducting filler network, *Composites Part A: Applied Science and Manufacturing*, 2020, **130**, 105763, doi: 10.1016/j.compositesa.2020.105763.
[32] H. Yang, L. H. Gong, Z. Zheng, X. F. Yao, Highly stretchable and sensitive conductive rubber composites with tunable piezoresistivity for motion detection and flexible electrodes, *Carbon*, 2020, **158**, 893-903, doi: 10.1016/j.carbon.2019.11.079.
[33] Y. Lu, D. Zhao, J. He, L. Zou, Armadillo-inspired ultra-sensitive flexible sensor for wearable electronics, *Chemical Engineering Journal*, 2023, **475**, 146171, doi: 10.1016/j.cej.2023.146171.
[34] J. H. Lee, J. Y. Bae, Y. N. Kim, M. Chae, W. J. Lee, J. Lee, I. D. Kim, J. K. Hyun, K. S. Lee, D. Kang, S. K. Kang, A fully biodegradable and ultra-sensitive crack-based strain sensor for biomechanical signal monitoring, *Advanced Functional Materials*, 2024, **34**, 2406035, doi: 10.1002/adfm.202406035.
[35] X. Cui, Y. Jiang, Z. Xu, M. Xi, Y. Jiang, P. Song, Y. Zhao, H. Wang, Stretchable strain sensors with dentate groove structure for enhanced sensing recoverability, *Composites Part B: Engineering*, 2021, **211**, 108641, doi: 10.1016/j.compositesb.2021.108641.
[36] J. Tang, Y. Wu, S. Ma, T. Yan, Z. Pan, Strain-sensing composite nanofiber filament and regulation mechanism of shoulder peaks based on carbon nanomaterial dispersion, *ACS Applied Materials & Interfaces*, 2023, **15**, 7392-7404, doi: 10.1021/acsami.2c20390.
[37] Y. Jiang, Z. Liu, N. Matsuhisa, D. Qi, W. R. Leow, H. Yang, J. Yu, G. Chen, Y. Liu, C. Wan, Z. Liu, X. Chen, Auxetic mechanical metamaterials to enhance sensitivity of stretchable strain sensors, *Advanced Materials*, 2018, **30**, 1706589, doi: 10.1002/adma.201706589.
[38] Y. Zhao, Y. Yang, B. Wan, T. Ding, X. Sha, Enhancement of the electric-force response of carbon black/silicone rubber composites by silane coupling agents, *Molecules*, 2024, **29**, 2740, doi: 10.3390/molecules29122740.
[39] H. Yang, L. Yuan, X. Yao, Z. Zheng, D. Fang, Monotonic strain sensing behavior of self-assembled carbon nanotubes/graphene silicone rubber composites under cyclic loading, *Composites Science and Technology*, 2020, **200**, 108474, doi: 10.1016/j.compscitech.2020.108474.
[40] X. Ji, Z. Lu, J. Wang, N. Ye, H. Zhang, L. Zhou, J. Li, Y. Lu, Construction of micro-nano hybrid structure based on carbon nanotube whisker and alumina for thermally conductive yet electrically insulating silicone rubber composites, *Composites Science and Technology*, 2024, **249**, 110495, doi: 10.1016/j.compscitech.2024.110495.
[41] X. Wang, Z. Yu, J. Hu, X. He, L. Zhang, A. Zhang, J. Zhang, Ultra-high conductivity double-conducting network elastomers with positive-negative pressure resistance constructed by self-assembly of fillers for intelligent sensing, *Chemical Engineering Journal*, 2024, **483**, 149260, doi: 10.1016/j.cej.2024.149260.
[42] H. Liu, J. Hu, W. Yang, J. Zhu, L. Fu, D. Li, L. Zhou, Honeycomb networks of boron nitride/nanodiamond with interlocking interfaces enhance the application reliability of silicone rubber thermal conductivity composites, *Polymer Composites*, 2024, **45**, 9064-9078, doi: 10.1002/pc.28394.
[43] J. Cui, F. Zeng, Y. Wang, A coarse-grained molecular dynamics study on the mechanical behavior of carbon nanotubes reinforced vulcanized natural rubber composites, *Polymer Composites*, 2023, **44**, 7752-7767, doi: 10.1002/pc.27662.
[44] Y. Li, R. Xing, Z. Li, C. Hou, B. Liu, F. Ren, Z. Wu, A molecular-dynamics-based model for the rate- and crosslink-density-dependent deformation of silicone rubber, *Computational Materials Science*, 2024, **231**, 112609, doi: 10.1016/j.commatsci.2023.112609.
[45] B. Yang, Y. Li, S. Wang, R. Nie, Q. Wang, Aminosilane modified graphene oxide for reinforcing nitrile butadiene rubber: Experiments and molecular dynamic simulations, *Composites Science and Technology*, 2023, **235**, 109956, doi: 10.1016/j.compscitech.2023.109956.

[46] W. Zou, J. Dong, Y. Luo, Q. Zhao, T. Xie, Dynamic covalent polymer networks: from old chemistry to modern day innovations, *Advanced Materials*, 2017, **29**, 1606100, doi: 10.1002/adma.201606100.
[47] Y. Yaoqi, Z. Zheng, S. Zhai, P. Zhang, The effects of roughness, temperature, and near-field thermal radiation on the thermal contact resistance between dissimilar materials Si, SiO_2 and SiC, *ES Energy & Environment*, 2023, **19**, 823, doi: 10.30919/esee8c823.
[48] N. Phupewkeaw, P. Sae-Oui, C. Sirisinha, Optimizing processing parameters for NR/EBC thermoplastic vulcanizates: a comprehensive full factorial design of experiments (DOE) strategy, *Polymers*, 2024, **16**, 1963, doi: 10.3390/polym16141963.
[49] J. Xiao, Z. Zhang, Y. Luan, S. Wu, Y. Wu, Influence of carbon black surface characteristics on CB-NR interfacial interaction: Molecular simulation and experimental study, *Composites Part A*: *Applied Science and Manufacturing*, 2024, **182**, 108198, doi: 10.1016/j.compositesa.2024.108198.
[50] L. Huang, Z. Song, X. Song, F. Yu, A. Lu, H. He, W. Liu, Z. Wang, P. Zhang, S. Li, X. Zhao, S. Cui, C. Zhu, Y. Liu, Performance enhancement of silicone rubber using superhydrophobic silica aerogel with robust nanonetwork structure and outstanding interfacial effect, *ACS Applied Materials & Interfaces*, 2024, **16**, 22580-22592, doi: 10.1021/acsami.4c03227.
[51] R. J. Sifri, O. Padilla-Vélez, G. W. Coates, B. P. Fors, Controlling the shape of molecular weight distributions in coordination polymerization and its impact on physical properties, *Journal of the American Chemical Society*, 2020, **142**, 1443-1448, doi: 10.1021/jacs.9b11462.
[52] M. Razavi-Nouri, M. Salavati, Effect of multi-walled carbon nanotubes on rheological behavior and electrical conductivity of poly(ethylene-co-vinyl acetate)/acrylonitrile-butadiene rubber/multi-walled carbon nanotubes nanocomposites, *Polymer Composites*, 2022, **43**, 8877-8889, doi: 10.1002/pc.27069.
[53] B. Wang, W. Tang, F. Zou, S. Liu, G. Li, X. Liao, Foaming behavior regulation of silicone rubber *via* evolution of crosslinked structure, *Sustainable Materials and Technologies*, 2023, **38**, e00764, doi: 10.1016/j.susmat.2023.e00764.
[54] C. Fengler, J. Keller, K. F. Ratzsch, M. Wilhelm, *In situ* RheoNMR correlation of polymer segmental mobility with mechanical properties during hydrogel synthesis, *Advanced Science*, 2022, **9**, 2104231, doi: 10.1002/advs.202104231.
[55] D. Presto, S. Narayanan, S. Moctezuma, M. Sutton, M. D. Foster, Microscopic origins of the nonlinear behavior of particle-filled rubber probed with dynamic strain XPCS, *ACS Applied Materials & Interfaces*, 2023, **15**, 22714-22729, doi: 10.1021/acsami.3c01955.
[56] D. Gabriel, A. Karbach, D. Drechsler, J. Gutmann, K. Graf, S. Kheirandish, Bound rubber morphology and loss tangent properties of carbon-black-filled rubber compounds, *Colloid and Polymer Science*, 2016, **294**, 501-511, doi: 10.1007/s00396-015-3802-6.
[57] N. Rasana, K. Jayanarayanan, H. T. Mohan, T. Keller, Static and dynamic mechanical properties of nanosilica and multiwalled carbon nanotube reinforced acrylonitrile butadiene styrene composites: theoretical mechanism of nanofiller reinforcement, *Iranian Polymer Journal*, 2021, **30**, 1211-1225, doi: 10.1007/s13726-021-00962-5.
[58] Q. Pan, G. Zhao, H. Deng, Q. Fu, Balanced physical properties for thermoplastic silicone vulcanizate-based polymer composites containing functional filler, *Polymer Composites*, 2020, **41**, 4307-4317, doi: 10.1002/pc.25713.
[59] Z. Li, X. Qi, L. Xu, H. Lu, W. Wang, X. Jin, Z. I. Md, Y. Zhu, Y. Fu, Q. Ni, Y. Dong, Self-repairing, large linear working range shape memory carbon nanotubes/ethylene vinyl acetate fiber strain sensor for human movement monitoring, *ACS Applied Materials & Interfaces*, 2020, **12**, 42179-42192, doi: 10.1021/acsami.0c12425.
[60] B. Zhou, Z. Liu, C. Li, L. Li, X. Zhang, Y. Sheng, Y. Zhou, L. Jiang, M. Tian, S. Chen, Fabrication of ultrasensitive and flexible strain sensor based on multi-wall carbon nanotubes coated electrospun styrene-ethylene-butylene-styrene block copolymer fibrous tubes, *European Polymer Journal*, 2022, **178**, 111501, doi: 10.1016/j.eurpolymj.2022.111501.
[61] S. Zhao, Y. Li, F. Wu, R. Hu, C. Deng, Humidity response of single carbon nanocoil and its temperature sensor independent of humidity and strain, *Applied Surface Science*, 2022, **605**, 154745, doi: 10.1016/j.apsusc.2022.154745.
[62] N. Wen, X. Guan, Z. Fan, Y. Guo, T. Cong, H. Huang, C. Li, J. Zhang, B. Lei, R. Yang, L. Liu, L. Pan, A highly stretchable and breathable self-powered dual-parameter sensor for decoupled temperature and strain sensing, *Organic Electronics*, 2023, **113**, 106723, doi: 10.1016/j.orgel.2022.106723.
[63] H. Wang, X. He, X. Huang, P. Su, T. Xia, W. Liu, Y. Ye, Vapor-based fabrication of PEDOT coating for wearable strain sensors with excellent sensitivity and self-cleaning capability, *Materials Today Chemistry*, 2023, **28**, 101361, doi: 10.1016/j.mtchem.2022.101361.
[64] S. Kim, B. Yoo, M. Miller, D. Bowen, D. J. Pines, K. M. Daniels, EGaIn-Silicone-based highly stretchable and flexible strain sensor for real-time two joint robotic motion monitoring, *Sensors and Actuators A*: *Physical*, 2022, **342**, 113659, doi: 10.1016/j.sna.2022.113659.